

ExtremeCast: Boosting Extreme Value Prediction for Global Weather Forecast

Wanghan Xu^{1,2} Kang Chen^{1,3} Tao Han^{1,4} Hao Chen¹ Wanli Ouyang¹ Lei Bai¹

Abstract

Data-driven weather forecast based on machine learning (ML) has experienced rapid development and demonstrated superior performance in the global medium-range forecast compared to traditional physics-based dynamical models. However, most of these ML models struggle with accurately predicting extreme weather, which is closely related to the extreme value prediction. Through mathematical analysis, we prove that the use of symmetric losses, such as the Mean Squared Error (MSE), leads to biased predictions and underestimation of extreme values. To address this issue, we introduce **Exloss**, a novel loss function that performs **asymmetric optimization** and highlights extreme values to obtain accurate extreme weather forecast. Furthermore, we introduce a **training-free** extreme value enhancement strategy named **ExEnsemble**, which increases the variance of pixel values and improves the forecast robustness. Combined with an advanced global weather forecast model, extensive experiments show that our solution can achieve state-of-the-art performance in extreme weather prediction, while maintaining the overall forecast accuracy comparable to the top medium-range forecast models.

1. Introduction

Weather forecast plays a crucial role in society and impacts various industries including energy (Meenal et al., 2022), agriculture (Fathi et al., 2022), and transportation (Wang et al., 2020a). In recent years, the field of Numerical Weather Prediction (NWP) has witnessed the rapid development of many data-driven forecast models based on machine learning (ML) (Kurth et al., 2023) (Lam et al., 2023) (Bi et al., 2023) (Chen et al., 2023a). These models are usually trained on extensive meteorological data spanning decades, achieving remarkable accuracy and fast inference.

¹Shanghai Artificial Intelligence Laboratory ²Xi'an Jiao Tong University ³University of Science and Technology of China ⁴The Hong Kong University of Science and Technology. Correspondence to: Lei Bai <bailei@pjlab.org.cn>.

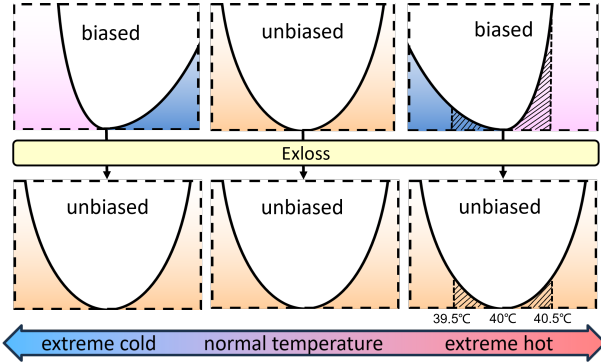


Figure 1. Why does MSE loss fail to predict extremes? It can be proved through extreme value theory that MSE loss provides a biased estimation of extreme values, leading to inevitable underestimation of extreme degree. In this paper, we propose an asymmetric loss function, Exloss, that corrects the bias.

Despite the advancements in ML forecast models, there remains a significant challenge when it comes to the extreme weather forecast. More specifically, these models tend to underestimate extreme values and produce smooth outputs, especially when the prediction lead time extends, which greatly hinders the prediction of natural disasters such as heatwaves and typhoons.

The underperformance of ML models in extreme weather prediction can be attributed to loss function during model training. Most ML models use Mean Squared Error (MSE) as the loss function, which aims to minimize the average error, improving the overall prediction accuracy at the expense of underfitting to extreme values.

In this paper, we present a new explanation from extreme value theory (EVT) to illustrate why the MSE-based models perform poorly in extreme weather prediction. Through mathematical analysis, we prove that in the case of data following an asymmetric extreme value distribution, underestimated predictions have a lower expectation of the total MSE loss compared to overestimated predictions, prompting the model to underestimate extreme values.

To tackle this issue, an **asymmetric** loss function, **Exloss**, is designed to correct this underestimation bias. Specifically, Exloss contains an asymmetric scaling function, which adjusts the distribution of the data to ensure that the expectations of the total MSE loss for both overestimated and

underestimated predictions are equal.

Exloss highlights the extreme values from the perspective of data distribution, but at the pixel-level, the predictions of the ML models may also have smoothing problem, with minimal variations between pixels. To address this problem, we propose a **parameter-free** and **training-free** module, **ExEnsemble**, which incorporates the rank histograms algorithm (Hamill, 2001) and the ensemble forecast (Gneiting & Raftery, 2005) to increase the variance of pixel values in the prediction, enhancing the extreme weather forecast without compromising overall accuracy.

Building upon an advanced medium-range global weather forecast model, i.e. FengWu (Chen et al., 2023a), and the diffusion (Ho et al., 2020) training strategy, we come up with ExtremeCast, a robust and powerful global weather forecast model that works on the 0.25° high-resolution. Trained with large-scale global atmosphere reanalysis dataset, i.e., ERA5 (Hersbach et al., 2020), ExtremeCast achieves state-of-the-art (SOTA) performance on extreme value metrics compared with both the top-performing data-driven global weather forecast models and the physics-based dynamic model, while maintaining the competitive overall accuracy. We summarize the contributions of this paper as follows:

- From the perspective of extreme value theory, we propose a new explanation for why MSE-based model is difficult to predict extreme values and prove that MSE leads to underestimation of extreme values.
- We design a novel loss function named **Exloss** based on an asymmetric design, which is able to eliminate the bias of the above underestimated forecasts and provide accurate extreme weather forecasts.
- We introduce **ExEnsemble**, a parameter-free and training-free module that leverages traditional weather forecast algorithms to improve the robustness of extreme weather forecasts.
- Large-scale experiments for global weather forecast on the 0.25° resolution show that our method significantly improve the forecasting ability of extreme weather, which is supported by obtaining better performance on extreme value metrics (e.g., RQE and SEDI) while maintaining the overall accuracy metrics (e.g., RMSE).

2. Related Work

2.1. Medium-range Weather Forecast

Medium-range weather forecast provides forecasts of weather conditions including temperature, wind speed, humidity, and more, for the next few days to two weeks. Traditional medium-range forecast models are mainly physics-based dynamic models such as the Integrated Forecasting

System (IFS) from European Centre for Medium-Range Weather Forecasts (ECMWF) (MODEL, 2003), whose development is primarily limited by the computational cost of numerical models (Ben-Bouallegue et al., 2023).

In recent years, data-driven models based on machine learning show significant potential for weather forecast (de Burgh-Day & Leeuwenburg, 2023). FourCastNet (Kurth et al., 2023) utilizes Adaptive Fourier Neural Operator networks (Guibas et al., 2021) for prediction and performs a two-step finetuning to improve the accuracy of autoregressive multi-step forecast, where the model's output is fed back as input for predicting the next step. This was followed by the Pangu-Weather (Bi et al., 2023), which uses 3D Swin-Transformer (Liu et al., 2021) and proposes hierarchical temporal aggregation aimed at reducing iterations in autoregressive forecast through the integration of multiple models. Subsequently, GraphCast (Lam et al., 2023) uses graph neural networks and performs a 12-step autoregressive finetuning. FengWu (Chen et al., 2023a) treats the prediction problem as a multi-task optimization and introduces a novel finetune strategy named replay buffer. FuXi (Chen et al., 2023b) reduces the cumulative error of the multi-step forecast by cascading three U-Transformer models (Petit et al., 2021) optimized at different lead times.

Although many ML models outperform ECMWF-IFS on the root mean square error (RMSE) metric, most of them suffer from the prediction smoothing issue and lag behind ECMWF-IFS on the extreme value metrics.

2.2. Extreme Weather Forecast

The application of ML models in predicting extreme weather remains relatively unexplored. Most existing models for extreme weather prediction are limited to regional scale or low resolution ($> 0.25^\circ$) rather than global scale and high resolution (0.25°). Zhao et al. (Zhao et al., 2003) use wavelet transform (Farge, 1992) to predict the occurrence of extreme weather, but cannot predict their actual values. Porto et al. (Porto et al., 2022) combine multiple models to address the challenge of learning diverse extreme weather patterns, which introduces a lot of additional training overhead and leads to potential gaps between different models. Lopez-Gomez et al. (Lopez-Gomez et al., 2023) increase the learning weight of extreme values by designing an exponential-based loss function. However, this method may cause exponential explosion in practical applications (Wang et al., 2019). Ni et al. (Ni, 2023) identify that using GAN loss (Creswell et al., 2018) can enhance the performance of the model in predicting extreme values, which is relatively difficult to optimize (Berard et al., 2019). Annau et al. (Annau et al., 2023) propose to separate high-frequency and low-frequency in the data through convolution and enhance the learning of high-frequency to improve extreme value pre-

dition. However, the learning of high-frequency is notably more challenging than low-frequency, which has not been effectively solved. Morozov et al. (Morozov et al., 2023) apply bias correction on extreme values through quantile regression, whose main limitation is that it only performs regression on seven discrete quantiles, which may not sufficiently capture the continuous distribution of the data.

For the global scale and high resolution extreme weather forecast, FuXi-Extreme (Zhong et al., 2023) uses a diffusion model to improve prediction accuracy of extreme weather. But the prediction robustness will be affected due to stochastic noise involved in the diffusion model, which can be improved by our proposed ExEnsemble module.

3. Method

3.1. Preliminary

Formally, we denote the weather state at time period i as a tensor $\mathcal{X}^i \in \mathbb{R}^{C \times H \times W}$, where C represents the number of atmospheric variables, H and W are the height and width. In this paper, we consider $C = 69$ atmospheric variables, which will be introduced in detail in Section 4.1. To align the experimental setup with ML models like Pangu-Weather (Bi et al., 2023) and GraphCast (Lam et al., 2023), we adopt a latitude and longitude resolution of 0.25° , which means the global atmospheric data is projected into a two-dimensional plane that $H = 721$ and $W = 1440$ horizontally.

The model learns to map from \mathcal{X}^i to \mathcal{X}^{i+1} with a time interval of 6 hours. Formally, it can be written as:

$$F_\theta(\mathcal{X}^i) = P(\mathcal{X}^{i+1} | \mathcal{X}^i) \quad (1)$$

where θ denotes the parameters of the model.

By iterating the above process n times, i.e. autoregressive prediction, the model can forecast any future time step \mathcal{X}^{i+n} ($n \in \mathbb{Z}$).

3.2. Model Framework Overview

Our model consists of two trainable modules and one training-free module. They are, respectively, a deterministic model denoted as M_d , a probabilistic generation model denoted as M_g , and a parameter-free module ExEnsemble. Specifically, M_d learns the mapping from \mathcal{X}^i to \mathcal{X}^{i+1} , followed by M_g , a conditional diffusion model that further enhances the details of M_d 's prediction. Finally, ExEnsemble module integrates and processes the outputs of M_d and M_g to obtain the final prediction.

In addition to one-step ($\mathcal{X}^i \rightarrow \mathcal{X}^{i+1}$) training, we also incorporate a finetuning of autoregressive regime to improve model's performance in multi-step prediction.

The process (including training and testing) of our model

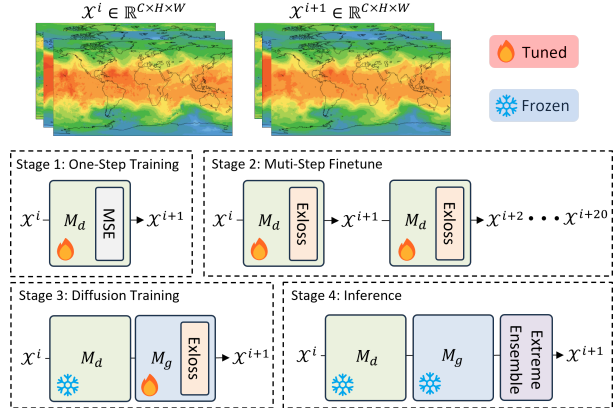


Figure 2. Model Framework.

can be divided into four distinct stages:

- Stage 1: One-Step pretraining. Use MSE loss to train M_d learning mapping from \mathcal{X}^i to \mathcal{X}^{i+1} as existing data-driven global weather forecasting models.
- Stage 2: Multi-Step finetuning. Use the proposed Exloss to finetune M_d learning autoregressive forecasting. This stage improves not only the accuracy of the model's multi-step predictions, but also the ability to predict extreme weather due to the use of Exloss.
- Stage 3: Diffusion training. Use Exloss to train M_g learning adding details to the output of M_d while freezing the parameters of M_d .
- Stage 4: Inference. In this stage, the ExEnsemble module that does not require training will be added for complete weather forecast, which further expends the variance of pixel values and enhances the forecast accuracy of extreme events.

In the following, we will start by analyzing the inherent limitations of MSE in predicting extreme values, followed by describing the details of the proposed Exloss and the ExEnsemble.

3.3. Why MSE Fails to Predict Extreme

For simplicity, we abbreviate Equation (1) as $F_\theta(X) = P(Y|X)$, where X is the input of the model, and Y is the target. Assume that the prior distribution of the data is a normal distribution $Y \sim \mathcal{N}(\mu, \sigma^2)$ (Kendall et al., 2018), where μ and σ are unknown. The process of model parameter optimization can be interpreted as maximum likelihood estimation (Jiang & Zhang, 2009) where the model predicts the mean μ of Y given X , as shown in Equation (2):

$$\underset{\theta}{\operatorname{argmax}} P(Y|\mu, \sigma^2), \text{ where } \mu \equiv F_\theta(X) \quad (2)$$

In fact, σ can also be estimated by model (Kendall et al., 2018). But for most regression models that only predict the

target, the estimation of σ is not performed. Thus, σ is commonly treated as a constant during analysis. Equation (2) can be transformed into Equation (3) by negative logarithm.

$$\begin{aligned}
& \underset{\theta}{\operatorname{argmin}} -\log (P(Y|\mu, \sigma^2)), \text{ where } \mu \equiv F_{\theta}(X) \\
&= \underset{\theta}{\operatorname{argmin}} -\log \left(\frac{1}{\sigma \sqrt{2\pi}} \exp \left(-\frac{(\mu - Y)^2}{2\sigma^2} \right) \right) \\
&= \underset{\theta}{\operatorname{argmin}} \frac{(\mu - Y)^2}{2\sigma^2} + \log (\sigma \sqrt{2\pi})
\end{aligned} \tag{3}$$

In the case where σ is not an optimization object, $\frac{1}{2\sigma^2}$ and $\log (\sigma \sqrt{2\pi})$ can be treated as constants, and the optimization problem ultimately transforms into Equation (4):

$$\underset{\theta}{\operatorname{argmin}} \text{MSE}(\mu, Y), \text{ where } \mu \equiv F_{\theta}(X) \tag{4}$$

Therefore, under the assumption that the data obeys a normal distribution, MSE loss can be interpreted as equivalent to maximum likelihood estimation.

However, this type of optimization has a significant negative impact on extreme values. Consider the introduction of a new variable, denoted as $Y_M = \max\{Y_1, Y_2, \dots, Y_n\}$, where $Y_i (i = 1, 2, \dots, n)$ represents different samples. In the context of weather forecasting, assuming that Y_1, Y_2, \dots, Y_n correspond to the temperatures in different regions, then Y_M represents the highest temperature in the world. According to the extreme value theory, Y_M obeys the extreme value distribution (more specifically, maximum value distribution), that is, $Y_M \sim G(\tilde{\mu}, \tilde{\sigma})$ (Kotz & Nadarajah, 2000), whose probability density function is:

$$f(Y_M) = \frac{1}{\tilde{\sigma}} \exp \left(-\frac{Y_M - \tilde{\mu}}{\tilde{\sigma}} - \exp \left(-\frac{Y_M - \tilde{\mu}}{\tilde{\sigma}} \right) \right) \tag{5}$$

where $\tilde{\mu}$ and $\tilde{\sigma}$ are its position and scale parameter respectively. It is worth mentioning that, unlike the normal distribution, the extreme value distribution is asymmetric. When employing maximum likelihood estimation for predicting the extreme value Y_M , we can derive the optimization objective through a similar procedure:

$$\begin{aligned}
& \underset{\theta}{\operatorname{argmin}} -\log (P(Y_M|\tilde{\mu}, \tilde{\sigma})) \\
&= \underset{\theta}{\operatorname{argmin}} \frac{Y_M - \tilde{\mu}}{\tilde{\sigma}} + \exp \left(-\frac{Y_M - \tilde{\mu}}{\tilde{\sigma}} \right) + \log (\tilde{\sigma}) \tag{6}
\end{aligned}$$

where $\tilde{\mu} \equiv \max \{F_{\theta}(X_1), F_{\theta}(X_2), \dots, F_{\theta}(X_n)\}$

Definition 3.1. Define the optimization function obtained through maximum likelihood estimation on the data of the maximum distribution as $obj_M(\cdot)$:

$$obj_M(\tilde{\mu}) = \frac{Y_M - \tilde{\mu}}{\tilde{\sigma}} + \exp \left(-\frac{Y_M - \tilde{\mu}}{\tilde{\sigma}} \right) + \log (\tilde{\sigma}) \tag{7}$$

It can be proved (in Appendix A.1) that the optimal solution of Equation (6), that is, the minimum of $obj_M(\cdot)$ is obtained if and only if $\tilde{\mu} = Y_M$, which meets the optimization goal. But due to the asymmetry of the data distribution, $obj_M(\cdot)$ is also asymmetric, as depicted in the upper left corner of Figure 1, which ultimately results in biased estimates.

Y_M can be viewed as a loss function that considers the data distribution. Under this assumption, the area enclosed by $obj_M(\cdot)$ and the x-coordinate axis can be regarded as the expectation of the total loss.

As illustrated in Figure 1, the shading on the left and the shading on the right represent the expectation of the total loss when model provides different estimates (underestimation and overestimation, respectively). Assuming the highest temperature in the world at a certain time is $Y_M = 40^{\circ}\text{C}$, predicting $\tilde{\mu} = 39.5^{\circ}\text{C}$ will get a lower loss than predicting $\tilde{\mu} = 40.5^{\circ}\text{C}$ based on probability expectation, which encourages the model to predict a smaller Y_M , that is $\tilde{\mu} = 39.5^{\circ}\text{C}$, rather than $\tilde{\mu} = 40.5^{\circ}\text{C}$. This finally results in underestimating the degree of extremes. The same situation occurs when predicting minimum values, such as the global minimum temperature. For a comprehensive analysis of $obj_M(\cdot)$, please refer to Appendix A.1.

In practice, the highest temperature predicted by the MSE-based model is always smaller than the true value (Ben-Bouallegue et al., 2023), which supports the above proof.

3.4. Exloss

Section 3.3 proves from the perspective of EVT that using MSE loss will underestimate the degree of extremes. To address this issue, a simple and straightforward idea is to make the originally asymmetric $obj_M(\cdot)$ symmetrical through scaling.

Of course, it is troublesome and unnecessary to transform $obj_M(\cdot)$ into a completely symmetric function. In actual operation, we use linear scaling to make the optimization objective function $obj_M(\cdot)$ symmetrical within a certain range ϵ , where ϵ is a hyperparameter that depends on both the data distribution and the accuracy of the model's predictions. In simple terms, when the model's predictions are highly accurate, the prediction error is smaller, allowing for the selection of a smaller value for ϵ . For detailed guidelines on selecting an appropriate value for ϵ , please refer to Appendix A.2. Mathematically, the process of achieving symmetry through scaling can be expressed as follows:

$$\begin{aligned} \tilde{\mu}_s &= \begin{cases} \frac{\tilde{\sigma}}{s_1}(\tilde{\mu} - Y_M) + Y_M, & \tilde{\mu} \leq Y_M \\ \frac{\tilde{\sigma}}{s_2}(\tilde{\mu} - Y_M) + Y_M, & \tilde{\mu} > Y_M \end{cases} \\ \text{s.t. } & \int_{\tilde{\mu}_s=Y_M-\epsilon}^{Y_M} obj_M(\tilde{\mu}_s) d\tilde{\mu}_s = \int_{\tilde{\mu}_s=Y_M}^{Y_M+\epsilon} obj_M(\tilde{\mu}_s) d\tilde{\mu}_s \end{aligned} \quad (8)$$

The purpose of the scaling factors s_1 and s_2 is to equalize the areas of the two shaded regions in Figure 1, which ensures that the expectations of the total loss are the same for underestimation and overestimation. Subsequently, s_1 and s_2 are combined into a function $S(\hat{\mathcal{Y}}, \mathcal{Y})$. By applying scaling function to the loss, we propose Exloss:

$$\begin{aligned} \text{Exloss}(\hat{\mathcal{Y}}, \mathcal{Y}) &= \|S(\hat{\mathcal{Y}}, \mathcal{Y}) \odot \hat{\mathcal{Y}} - S(\hat{\mathcal{Y}}, \mathcal{Y}) \odot \mathcal{Y}\|^2 \\ &= \|S(\hat{\mathcal{Y}}, \mathcal{Y}) \odot (\hat{\mathcal{Y}} - \mathcal{Y})\|^2 \end{aligned} \quad (9)$$

where $\hat{\mathcal{Y}}$ and \mathcal{Y} represent the model prediction and the target respectively, $S(\hat{\mathcal{Y}}, \mathcal{Y}) \in \mathbb{R}^{C \times H \times W}$ is **asymmetrical** scaling function. For the detailed form of $S(\hat{\mathcal{Y}}, \mathcal{Y})$, please refer to the Appendix A.2

In fact, by calculating $S(\hat{\mathcal{Y}}, \mathcal{Y})$, it can be observed that Exloss increases the loss weight when the model underestimates extreme value. This behavior is highly rational, as it adaptively increases the penalty for underestimations.

3.5. ExEnsemble

Some prior studies, including (Rasp & Lerch, 2018) and (Scher & Messori, 2021), have employed ensemble forecast (Gneiting & Raftery, 2005) in ML models to improve the forecast accuracy and the robustness to initial condition uncertainty (Du et al., 2018). Specifically, multiple perturbations are introduced to the model input, generating multiple forecast outcomes that are subsequently averaged to produce the model's output. While ensemble mean can improve forecast accuracy, it tends to diminish the strength of extreme values due to the averaging operation involved.

In this work, we propose to use the ensemble strategy from a different perspective and boost the prediction ability of extreme values. To obtain more extreme ensemble forecasts, we propose the ExEnsemble, drawing insights from rank histograms algorithm (Hamill, 2001). The process begins by introducing noise to the input, generating m ensemble results. Rather than using an averaging approach, we sort the pixel values from all ensembles, followed by dividing the sorted results into groups of m . Finally, replace the original pixel value with the median value of the ranking interval corresponding to each pixel.

As depicted in Figure 3, ExEnsemble adaptively expands the

range of pixel values without altering the overall distribution, thereby producing more extreme predictions. Furthermore, ensemble generates multiple forecast results, where the forecast errors offset each other probabilistically, for which it improves the robustness against the initial condition uncertainty (Du et al., 2018). For detailed implementation, please refer to Appendix A.3.

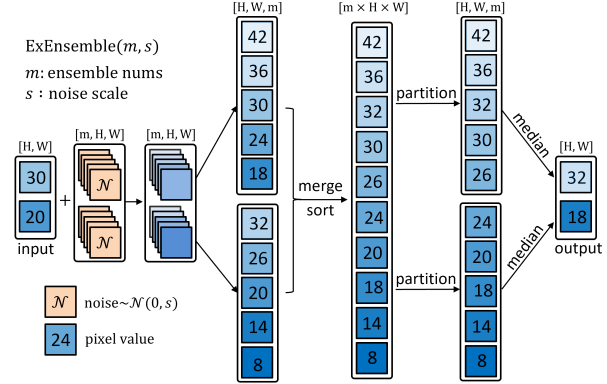


Figure 3. ExEnsemble.

4. Experiment

4.1. Experimental Setup

Dataset. The training process utilizes the 5th generation of ECMWF reanalysis (ERA5) data (Hersbach et al., 2020). We use the data from 1979 to 2017 as the training set, from 2018 to 2021 as the validation set, and from 2022 to 2022 as the test set. Our model employs 69 atmospheric variables, including four surface variables and five upper-level variables with 13 pressure levels, as shown in Section 4.1.

Name	Description	Levels
u10	X-direction wind at 10m height	Single
v10	Y-direction wind at 10m height	Single
t2m	Temperature at 2m height	Single
msl	Mean sea level pressure	Single
z	Geopotential	13
q	Absolute humidity	13
u	X-direction wind	13
v	Y-direction wind	13
t	Temperature	13

Table 1. Atmospheric Variables Considered. The 13 levels are 50, 100, 150, 200, 250, 300, 400, 500, 600, 700, 850, 925, 1000hPa.

Network Structure. M_d has the same network structure as (Chen et al., 2023a), which uses Swin-Transformer (Vaswani et al., 2017) as the backbone, and designs the structure of encoder and decoder through down-sampling and up-sampling. M_g uses a mainstream diffusion implementation (Wang, 2020) which use a U-Transformer (Petit et al., 2021) as backbone, and realizes conditional generation by concatenating condition to the model input.

Baseline Models. We choose five ML models, namely

Pangu (Bi et al., 2023), GraphCast (Lam et al., 2023), FengWu (Chen et al., 2023a), FuXi (Chen et al., 2023b), FuXi-Extreme (Zhong et al., 2023) and a physics-based dynamic model ECMWF-IFS (MODEL, 2003), as the baseline models for comparative experiments. For detailed introductions of these models, please refer to Section 2.

Metrics. We use three metrics to reflect the extreme weather forecast performance and the overall accuracy.

- **RQE.** Relative Quantile Error (Kurth et al., 2023). It is defined as the relative error of large quantiles (ranging from 90% to 99.99%) between prediction and target. A positive RQE value indicates that extreme values are overestimated, while a negative RQE value indicates that extreme values are underestimated.
- **SEDI.** Symmetric Extremal Dependency Index (Ferro & Stephenson, 2011). By classifying each pixel into extreme weather or normal weather, this metric calculates the hit rate of the classification. In addition, by selecting different thresholds, SEDI for different degrees of extreme weather can be calculated, such as SEDI 90th, SEDI 95th, etc (Zhong et al., 2023). A higher SEDI value closer to 1 indicates better prediction accuracy for extreme values.
- **RMSE.** Weighted Root Mean Square Error (Rasp et al., 2020). It is calculated by applying latitude-related weights to the root mean square error, which reflects the overall forecast error. A smaller RMSE value indicates a higher forecast accuracy.

Both RQE and SEDI serve as metrics to evaluate the accuracy of extreme value predictions, but their focus is different. RQE reflects more on the global scale, while SEDI reflects more on the regional (pixel-level) scale.

4.2. Global Extreme Weather Forecast Capability

We use the RQE to evaluate the models' ability to predict extreme values on the global scale. As depicted in Figure 4, the RQE values of most ML models exhibit a tendency to become progressively more negative as the lead time increases, indicating an increasing underestimation of extreme values. On the contrary, the dynamic model has a relatively better RQE, that is, an RQE value closer to 0, and does not decrease as the lead time increases.

For our model, overall, the RQE does not decrease as the lead time increases, which is due to Exloss's asymmetric optimization, avoiding the underestimation of extreme values. Especially for q500 (the channel of absolute humidity at the 500hPa pressure layer), u500, and u10, our model predicts with a RQE close to 0 consistently, surpassing both ML models and the dynamic model, showing the accurate and stable extreme value prediction capabilities.

Our model slightly overestimates (around 10^{-3}) the ex-

treme values in certain atmospheric variables like z500 and t2m, which is very rare for ML models but is occasionally observed in dynamic models as well. Appropriate overestimation can provide a more adequate upper bound for the prediction of extreme events, which is beneficial for some applications, such as probabilistic forecasting (Gneiting & Katzfuss, 2014).

4.3. Regional Extreme Weather Forecast Capability

Different from RQE, SEDI focus more on extreme values in local areas. This is because each pixel uses its quantile in the time dimension as a threshold, and this threshold is different from month to month. For instance, a temperature of -10°C may not be considered as an extreme event for high-latitude areas during winter, but it could be extreme for mid-latitude areas in summer.

As illustrated in Figure 5, for surface temperature, our model's prediction accuracies at 90th, 95th, 98th extreme degrees are significantly higher than that of other models. Regarding the most extreme scenarios at the 99.5th quantile, our model demonstrates relatively better performance when the lead time is less than 24 hours, and for lead times exceeding 24 hours, our model has similar performance to FuXi-Extreme and ECMWF-IFS.

For surface wind speed, our model significantly outperforms other models across all extreme levels. It is worth noting that the SEDI of our model's first step prediction (with a lead time of 6 hours) is remarkably high, predominantly exceeding 0.95. This is particularly challenging for wind speed which exhibit rapid and diverse changes, highlighting the excellent performance of our model in forecasting extreme wind speeds.

4.4. Case Analysis

To better showcase the performance of our model, we select two natural disasters, typhoon and heatwave, for visual analysis. Specifically, we choose the Nanmadol typhoon (Wu et al., 2023) at 6:00 on September 17, 2022, and the heatwave in the southeastern coastal area of China at 12:00 on August 14, 2022 (Jiang et al., 2023), for three-day forecast and visualization. Figure 7 illustrates the results, with the two rows showing surface wind speed and surface temperature, respectively.

Regarding typhoons, the wind speeds of our prediction are the most extreme and closest to the real wind speeds. This aligns with the findings observed in the far-leading SEDI of wind speed in Section 4.3, showing the exceptional performance of our model in predicting extreme wind speeds. This capability is of significant importance for estimating the intensity of typhoon landings and assessing the potential damage to coastal areas.

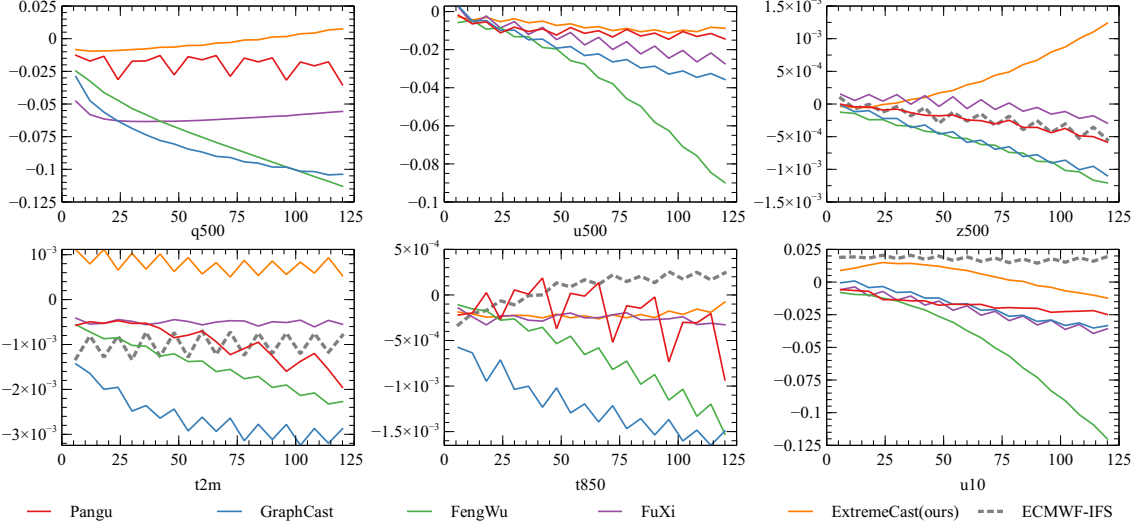


Figure 4. RQE ($RQE < 0$ means underestimating extreme values, $RQE > 0$ means overestimating extreme values). All results are tested on 2018 data and use ERA5 as the target.

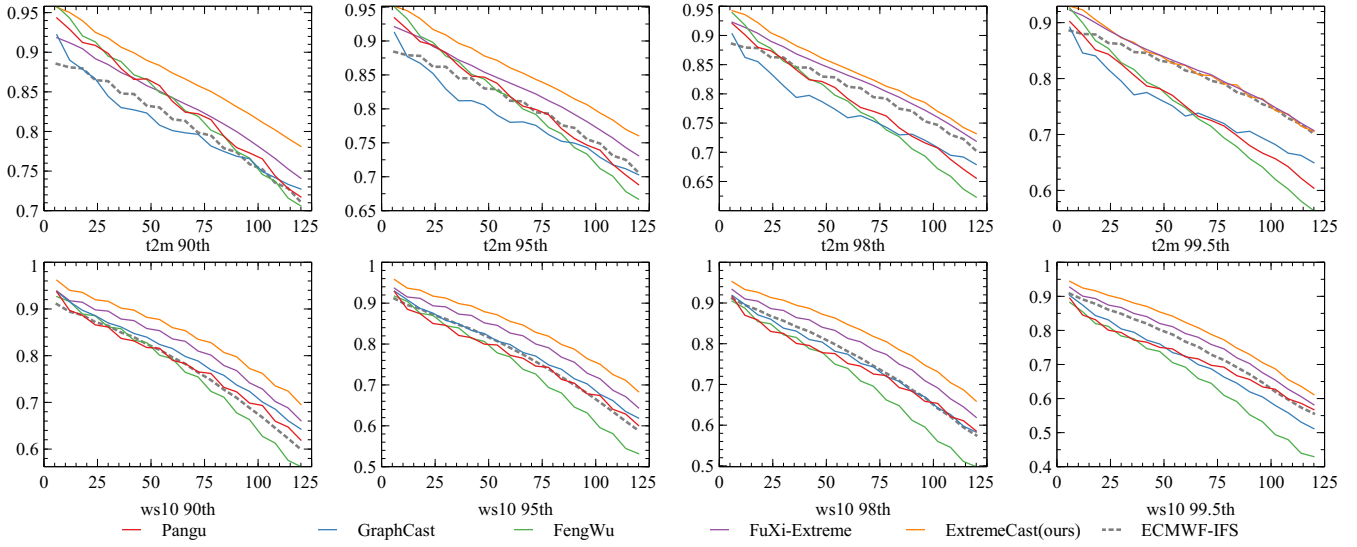


Figure 5. SEDI (the closer to 1 the better). ws10 represents surface wind speed, that is, $ws10 = \sqrt{u10^2 + v10^2}$. All results are tested on 2018 data and use ERA5 as the target.

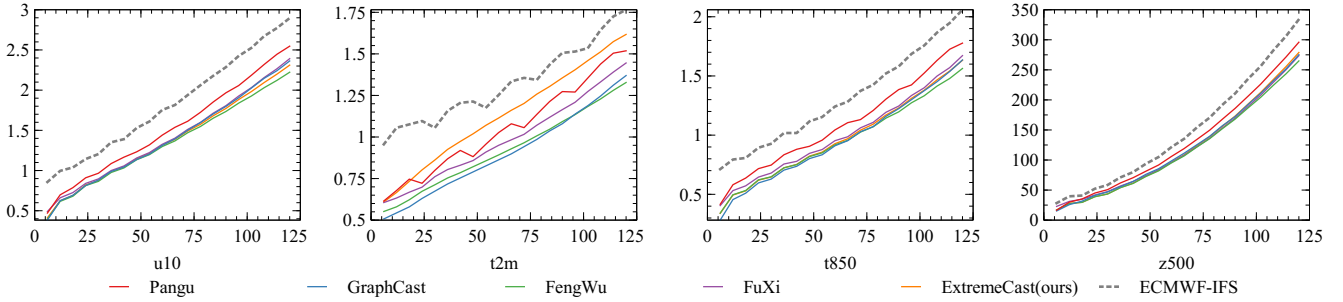


Figure 6. RMSE (the smaller the better). All results are tested on 2018 data and use ERA5 as the target.

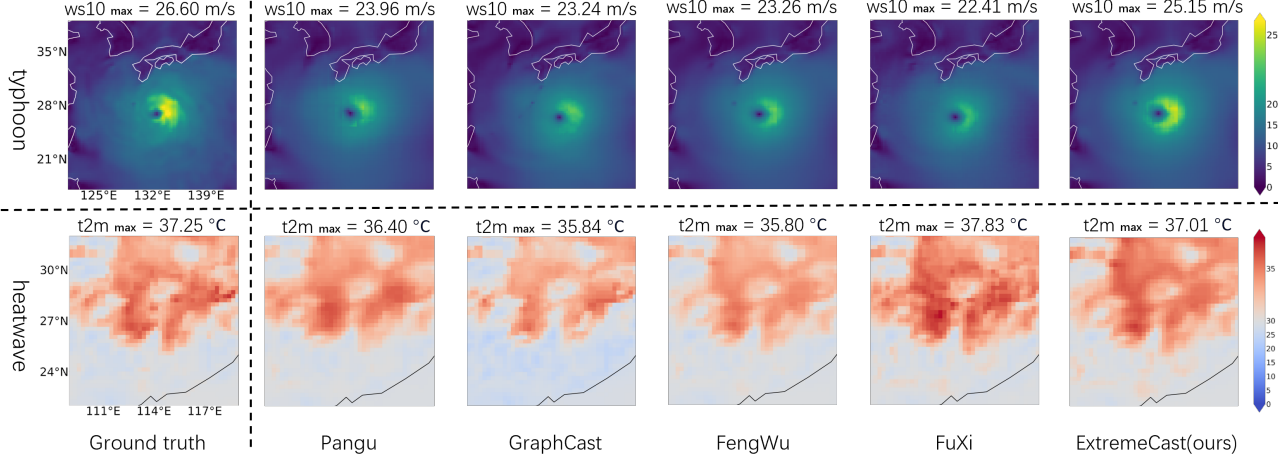


Figure 7. Three-day Typhoon and Heatwave Forecast Visualization. The model input and ground truth are from ERA5. Color bars are consistent across all pictures to ensure fairness.

Exloss	Diffusion	ExEnsemble	RQE (- underestimate, + overestimate)				SEDI (the closer to 1 the better)			
			t2m	u10	q500	u500	t2m@90th	t2m@99.5th	ws10@90th	ws10@99.5th
①	x	x	-0.0023	-0.1201	-0.1130	-0.0899	0.7059	0.5637	0.5623	0.4295
②	✓	x	-0.0012	-0.0792	-0.0330	-0.0538	0.7589	0.6222	0.6423	0.5156
③	x	✓	+0.0005	-0.0296	-0.0407	-0.0299	0.7743	0.6947	0.6793	0.5778
④	✓	x	-0.0007	-0.0374	+0.0063	-0.0173	0.7643	0.6405	0.6791	0.5773
⑤	✓	✓	+0.0002	-0.0496	-0.0291	-0.0459	0.7764	0.6927	0.6627	0.5517
⑥	✓	✓	+0.0008	-0.0120	+0.0092	-0.0125	0.7796	0.7106	0.6930	0.6056

Table 2. Ablation Experiment. All results are predictions on the fifth day and use ERA5 as the target.

In the case of the heatwave, both of the predictions of our model and FuXi-Extreme are more extreme than other models. Although fuxi-extreme’s predictions are more extreme than ours, our model gets a prediction (37.01°C) that is closer to the true value (37.25°C) for the regional maximum temperature prediction.

4.5. Ablation Experiment

We assess the individual contributions of each module by conducting ablation experiments where we remove Exloss, and ExEnsemble. Additionally, as an effective part of the model implementation, diffusion model is also considered in the ablation experiment.

Through Table 2, we find that all three modules are beneficial in enhancing the prediction of extreme values. Specifically, we discover that the asymmetric optimization of Exloss plays a crucial role in enhancing the forecasting capabilities of extreme weather events. This is evident from the comparison between row ① and row ②, where the use of Exloss leads to significant improvements in both RQE and SEDI metrics. Furthermore, as observed in row ③, the removal of Exloss results in a significant decrease in all metrics compared to the best version indicated in row ⑥.

Moreover, Diffusion and ExEnsemble have great improvements in the prediction of extreme temperatures and extreme wind speeds respectively, which highlights the favorable decoupling properties of different modules in our model.

4.6. Normal Weather Forecast Capability

Although the focus of this paper is extreme weather prediction, the overall forecast accuracy of our model is still competitive. As shown in Figure 6, while our model demonstrates outstanding performance in predicting extreme wind speeds, it also achieves a high accuracy in overall wind speed prediction, as indicated by RMSE u10. Additionally, the RMSE metrics of our model on other variables are also comparable to top ML models and surpass ECMWF-IFS.

5. Conclusions

Weather forecast models based on machine learning often face challenges in accurately predicting extreme weather. In this paper, we provide an explanation, based on extreme value theory, for the inherent limitations of MSE-based models in forecasting extreme values. To address this issue, a novel loss function called Exloss is introduced, which rectifies deviations in extreme value prediction through asymmetric optimization.

Moreover, we propose a training-free module named ExEnsemble that promotes extreme values at the pixel-level, enhancing the model’s capability in predicting extreme weather events. Experimental results show that our model, ExtremeCast, achieves SOTA performance in extreme value metrics such as RQE and SEDI, while maintaining the competitive overall accuracy.

References

Annau, N. J., Cannon, A. J., and Monahan, A. H. Algorithmic hallucinations of near-surface winds: Statistical downscaling with generative adversarial networks to convection-permitting scales. *Artificial Intelligence for the Earth Systems*, 2(4):e230015, 2023.

Bellprat, O. and Doblas-Reyes, F. Attribution of extreme weather and climate events overestimated by unreliable climate simulations. *Geophysical Research Letters*, 43(5):2158–2164, 2016.

Ben-Bouallegue, Z., Clare, M. C., Magnusson, L., Gascon, E., Maier-Gerber, M., Janousek, M., Rodwell, M., Pinault, F., Dramsch, J. S., Lang, S. T., et al. The rise of data-driven weather forecasting. *arXiv preprint arXiv:2307.10128*, 2023.

Berard, H., Gidel, G., Almahairi, A., Vincent, P., and Lacoste-Julien, S. A closer look at the optimization landscapes of generative adversarial networks. *arXiv preprint arXiv:1906.04848*, 2019.

Bi, K., Xie, L., Zhang, H., Chen, X., Gu, X., and Tian, Q. Accurate medium-range global weather forecasting with 3d neural networks. *Nature*, 619(7970):533–538, 2023.

Cai, Y. and Hames, D. Minimum sample size determination for generalized extreme value distribution. *Communications in Statistics—Simulation and Computation®*, 40(1): 87–98, 2010.

Chen, K., Han, T., Gong, J., Bai, L., Ling, F., Luo, J.-J., Chen, X., Ma, L., Zhang, T., Su, R., et al. Fengwu: Pushing the skillful global medium-range weather forecast beyond 10 days lead. *arXiv preprint arXiv:2304.02948*, 2023a.

Chen, L., Zhong, X., Zhang, F., Cheng, Y., Xu, Y., Qi, Y., and Li, H. Fuxi: A cascade machine learning forecasting system for 15-day global weather forecast. *arXiv preprint arXiv:2306.12873*, 2023b.

Creswell, A., White, T., Dumoulin, V., Arulkumaran, K., Sengupta, B., and Bharath, A. A. Generative adversarial networks: An overview. *IEEE signal processing magazine*, 35(1):53–65, 2018.

de Burgh-Day, C. O. and Leeuwenburg, T. Machine learning for numerical weather and climate modelling: a review. *Geoscientific Model Development*, 16(22):6433–6477, 2023.

Du, J., Berner, J., Buizza, R., Charron, M., Houtekamer, P. L., Hou, D., Jankov, I., Mu, M., Wang, X., Wei, M., et al. Ensemble methods for meteorological predictions. *noaa*, 2018.

Fang, W., Xue, Q., Shen, L., and Sheng, V. S. Survey on the application of deep learning in extreme weather prediction. *Atmosphere*, 12(6):661, 2021.

Farge, M. Wavelet transforms and their applications to turbulence. *Annual review of fluid mechanics*, 24(1):395–458, 1992.

Fathi, M., Hagh Kashani, M., Jameii, S. M., and Mahdipour, E. Big data analytics in weather forecasting: A systematic review. *Archives of Computational Methods in Engineering*, 29(2):1247–1275, 2022.

Ferro, C. A. and Stephenson, D. B. Extremal dependence indices: Improved verification measures for deterministic forecasts of rare binary events. *Weather and Forecasting*, 26(5):699–713, 2011.

Francis, J. A. and Vavrus, S. J. Evidence linking arctic amplification to extreme weather in mid-latitudes. *Geophysical research letters*, 39(6), 2012.

Gneiting, T. and Katzfuss, M. Probabilistic forecasting. *Annual Review of Statistics and Its Application*, 1:125–151, 2014.

Gneiting, T. and Raftery, A. E. Weather forecasting with ensemble methods. *Science*, 310(5746):248–249, 2005.

Gray, W. M. Tropical cyclone genesis in the western north pacific. *Journal of the Meteorological Society of Japan. Ser. II*, 55(5):465–482, 1977.

Guibas, J., Mardani, M., Li, Z., Tao, A., Anandkumar, A., and Catanzaro, B. Adaptive fourier neural operators: Efficient token mixers for transformers. *arXiv preprint arXiv:2111.13587*, 2021.

Hamill, T. M. Interpretation of rank histograms for verifying ensemble forecasts. *Monthly Weather Review*, 129(3): 550–560, 2001.

Hernández-Orallo, J., Flach, P., and Ferri Ramírez, C. A unified view of performance metrics: Translating threshold choice into expected classification loss. *Journal of Machine Learning Research*, 13:2813–2869, 2012.

Hersbach, H., Bell, B., Berrisford, P., Hirahara, S., Horányi, A., Muñoz-Sabater, J., Nicolas, J., Peubey, C., Radu, R., Schepers, D., et al. The era5 global reanalysis. *Quarterly Journal of the Royal Meteorological Society*, 146(730): 1999–2049, 2020.

Ho, J., Jain, A., and Abbeel, P. Denoising diffusion probabilistic models. *Advances in neural information processing systems*, 33:6840–6851, 2020.

Jiang, J., Liu, Y., Mao, J., and Wu, G. Extreme heatwave over eastern china in summer 2022: the role of three oceans and local soil moisture feedback. *Environmental Research Letters*, 18(4):044025, 2023.

Jiang, W. and Zhang, C.-H. General maximum likelihood empirical bayes estimation of normal means. *projecteuclid*, 2009.

Kendall, A., Gal, Y., and Cipolla, R. Multi-task learning using uncertainty to weigh losses for scene geometry and semantics. In *Proceedings of the IEEE conference on computer vision and pattern recognition*, pp. 7482–7491, 2018.

Kotz, S. and Nadarajah, S. *Extreme value distributions: theory and applications*. world scientific, 2000.

Kurth, T., Subramanian, S., Harrington, P., Pathak, J., Mardani, M., Hall, D., Miele, A., Kashinath, K., and Anandkumar, A. Fourcastnet: Accelerating global high-resolution weather forecasting using adaptive fourier neural operators. In *Proceedings of the Platform for Advanced Scientific Computing Conference*, pp. 1–11, 2023.

Lam, R., Sanchez-Gonzalez, A., Willson, M., Wirnsberger, P., Fortunato, M., Alet, F., Ravuri, S., Ewalds, T., Eaton-Rosen, Z., Hu, W., et al. Learning skillful medium-range global weather forecasting. *Science*, pp. eadi2336, 2023.

Liu, Z., Lin, Y., Cao, Y., Hu, H., Wei, Y., Zhang, Z., Lin, S., and Guo, B. Swin transformer: Hierarchical vision transformer using shifted windows. In *Proceedings of the IEEE/CVF international conference on computer vision*, pp. 10012–10022, 2021.

Lopez-Gomez, I., McGovern, A., Agrawal, S., and Hickey, J. Global extreme heat forecasting using neural weather models. *Artificial Intelligence for the Earth Systems*, 2(1):e220035, 2023.

Meenal, R., Binu, D., Ramya, K., Michael, P. A., Vinoth Kumar, K., Rajasekaran, E., and Sangeetha, B. Weather forecasting for renewable energy system: A review. *Archives of Computational Methods in Engineering*, 29(5):2875–2891, 2022.

MODEL, E. W. Ifs documentation. *ecmwf*, 2003.

Morozov, V., Galliamov, A., Lukashevich, A., Kurdukova, A., and Maximov, Y. Cmip x-mos: Improving climate models with extreme model output statistics. *arXiv preprint arXiv:2311.03370*, 2023.

Ni, Z. Kunyu: A high-performing global weather model beyond regression losses. *arXiv preprint arXiv:2312.08264*, 2023.

Petit, O., Thome, N., Rambour, C., Themyr, L., Collins, T., and Soler, L. U-net transformer: Self and cross attention for medical image segmentation. In *Machine Learning in Medical Imaging: 12th International Workshop, MLMI 2021, Held in Conjunction with MICCAI 2021, Strasbourg, France, September 27, 2021, Proceedings 12*, pp. 267–276. Springer, 2021.

Porto, F., Ferro, M., Ogasawara, E., Moeda, T., de Barros, C. D. T., Silva, A. C., Zorrilla, R., Pereira, R. S., Castro, R. N., Silva, J. V., et al. Machine learning approaches to extreme weather events forecast in urban areas: Challenges and initial results. *Supercomputing Frontiers and Innovations*, 9(1):49–73, 2022.

Rasp, S. and Lerch, S. Neural networks for postprocessing ensemble weather forecasts. *Monthly Weather Review*, 146(11):3885–3900, 2018.

Rasp, S., Dueben, P. D., Scher, S., Weyn, J. A., Mouatadid, S., and Thuerey, N. Weatherbench: a benchmark data set for data-driven weather forecasting. *Journal of Advances in Modeling Earth Systems*, 12(11):e2020MS002203, 2020.

Richard, Y., Rouault, M., Pohl, B., Crétat, J., Duclot, I., Taboulot, S., Reason, C., Macron, C., and Buiron, D. Temperature changes in the mid-and high-latitudes of the southern hemisphere. *International Journal of Climatology*, 33(8):1948–1963, 2013.

Scher, S. and Messori, G. Ensemble methods for neural network-based weather forecasts. *Journal of Advances in Modeling Earth Systems*, 13(2), 2021.

Vaswani, A., Shazeer, N., Parmar, N., Uszkoreit, J., Jones, L., Gomez, A. N., Kaiser, Ł., and Polosukhin, I. Attention is all you need. *Advances in neural information processing systems*, 30, 2017.

Wang, H.-W., Peng, Z.-R., Wang, D., Meng, Y., Wu, T., Sun, W., and Lu, Q.-C. Evaluation and prediction of transportation resilience under extreme weather events: A diffusion graph convolutional approach. *Transportation research part C: emerging technologies*, 115:102619, 2020a.

Wang, P. denoising-diffusion-pytorch. [url](#), 2020. Accessed: 2020-09-06.

Wang, Q., Ma, Y., Zhao, K., and Tian, Y. A comprehensive survey of loss functions in machine learning. *Annals of Data Science*, pp. 1–26, 2020b.

Wang, S., Li, Y., Liang, X., Quan, D., Yang, B., Wei, S., and Jiao, L. Better and faster: Exponential loss for image patch matching. In *Proceedings of the IEEE/CVF International Conference on Computer Vision*, pp. 4812–4821, 2019.

Wei, C.-C., Peng, P.-C., Tsai, C.-H., and Huang, C.-L. Regional forecasting of wind speeds during typhoon landfall in taiwan: A case study of westward-moving typhoons. *Atmosphere*, 9(4):141, 2018.

Wellander, N., Lundén, O., and Backstrom, M. The maximum value distribution in a reverberation chamber. In *2001 IEEE EMC International Symposium. Symposium Record. International Symposium on Electromagnetic Compatibility (Cat. No. 01CH37161)*, volume 2, pp. 751–756. IEEE, 2001.

Wu, Z., Zhang, Y., Zhang, L., and Zheng, H. Interaction of cloud dynamics and microphysics during the rapid intensification of super-typhoon nannadol (2022) based on multi-satellite observations. *Geophysical Research Letters*, 50(15):e2023GL104541, 2023.

Yang, L., Zhang, Z., Song, Y., Hong, S., Xu, R., Zhao, Y., Zhang, W., Cui, B., and Yang, M.-H. Diffusion models: A comprehensive survey of methods and applications. *ACM Computing Surveys*, 56(4):1–39, 2023.

Yang, T.-H. and Tsai, C.-C. Using numerical weather model outputs to forecast wind gusts during typhoons. *Journal of Wind Engineering and Industrial Aerodynamics*, 188: 247–259, 2019.

Zhao, J., Lu, C.-T., and Kou, Y. Detecting region outliers in meteorological data. In *Proceedings of the 11th ACM international symposium on Advances in geographic information systems*, pp. 49–55, 2003.

Zhong, X., Chen, L., Liu, J., Lin, C., Qi, Y., and Li, H. Fuxi-extreme: Improving extreme rainfall and wind forecasts with diffusion model. *arXiv preprint arXiv:2310.19822*, 2023.

A. Appendix

A.1. Analysis of the Optimization Objective

First, we examine the optimization function for the scenario where the model predicts the maximum value $Y_M = \max\{Y_1, Y_2, \dots, Y_n\}$. In this case, Y_M follows a maximum distribution, characterized by its probability density function (Wellander et al., 2001):

$$f(Y_M) = \frac{1}{\tilde{\sigma}} \exp\left(-\frac{Y_M - \tilde{\mu}}{\tilde{\sigma}} - \exp\left(-\frac{Y_M - \tilde{\mu}}{\tilde{\sigma}}\right)\right) \quad (10)$$

where $\tilde{\mu}$ and $\tilde{\sigma}$ are its position and scale parameter respectively. Unlike the normal distribution, maximum distribution is an asymmetric skewed distribution. We can draw a histogram of the maximum distribution through the following algorithm, so as to observe the characteristics of the maximum distribution more directly.

Algorithm 1 Maximum Distribution Sample

```

 $M = []$  # List of maximum distribution sampling
for  $i = 1$  to 10000 do
     $N = []$  # List of normal distribution sampling
    for  $j = 1$  to 10000 do
         $x \leftarrow \mathcal{N}(0, 1)$ 
         $N.append(x)$ 
    end for
     $x_M \leftarrow \text{Max}(N)$ 
     $M.append(x_M)$ 
end for

```

Draw a histogram of M and N .

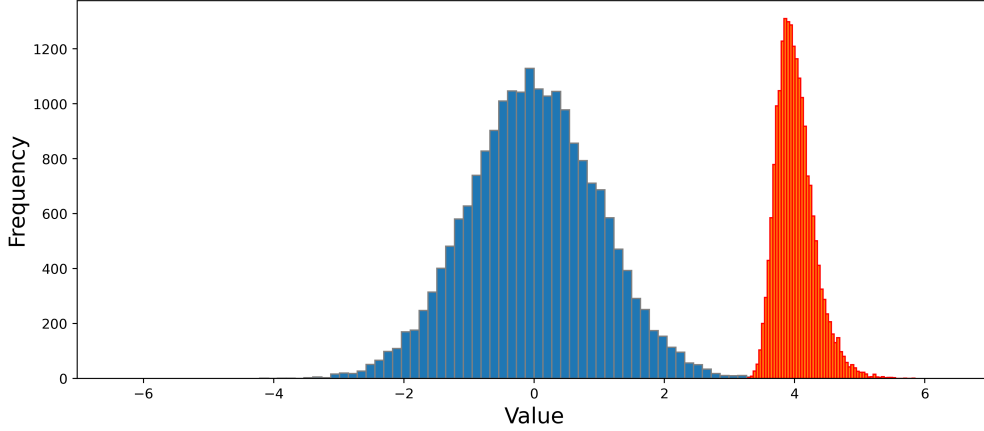


Figure 8. Visualization of Maximum Distribution and Normal Distribution. The blue histogram is sampled from the normal distribution, and the red histogram is sampled from the maximum distribution.

The asymmetry of the distribution of maximum values can be clearly seen from Figure 8. This asymmetry is also the focus of our discussion below.

When making predictions for the extreme value Y_M , the optimization objective can be formulated as follows:

$$\begin{aligned}
& \underset{\theta}{\operatorname{argmin}} -\log (P(Y_M|\tilde{\mu}, \tilde{\sigma})) \\
&= \underset{\theta}{\operatorname{argmin}} \frac{Y_M - \tilde{\mu}}{\tilde{\sigma}} + \exp\left(-\frac{Y_M - \tilde{\mu}}{\tilde{\sigma}}\right) + \log(\tilde{\sigma}) \\
& \text{where } \tilde{\mu} \equiv \max\{F_{\theta}(X_1), F_{\theta}(X_2), \dots, F_{\theta}(X_n)\}
\end{aligned} \tag{11}$$

Denote the optimization objective as $obj_M(\cdot)$:

$$obj_M(\tilde{\mu}) = \frac{Y_M - \tilde{\mu}}{\tilde{\sigma}} + \exp\left(-\frac{Y_M - \tilde{\mu}}{\tilde{\sigma}}\right) + \log(\tilde{\sigma}) \tag{12}$$

The derivative of $obj_M(\cdot)$ with respect to $\tilde{\mu}$ is:

$$obj'_M(\tilde{\mu}) = -\frac{1}{\tilde{\sigma}} + \frac{1}{\tilde{\sigma}} \exp\left(-\frac{Y_M - \tilde{\mu}}{\tilde{\sigma}}\right) \tag{13}$$

Its second derivative is:

$$obj''_M(\tilde{\mu}) = \frac{1}{\tilde{\sigma}^2} \exp\left(-\frac{Y_M - \tilde{\mu}}{\tilde{\sigma}}\right) \tag{14}$$

Its second derivative $obj''_M(\tilde{\mu})$ is positive, indicating that the derivative, $obj'_M(\tilde{\mu})$, monotonically increases. As $obj'_M(Y_M) = 0$, we can conclude that:

$$\begin{cases} obj'_M(\tilde{\mu}) < 0, \tilde{\mu} < Y_M \\ obj'_M(\tilde{\mu}) = 0, \tilde{\mu} = Y_M \\ obj'_M(\tilde{\mu}) > 0, \tilde{\mu} > Y_M \end{cases} \tag{15}$$

So $obj_M(\tilde{\mu})$ first decreases and then increases, with its minimum value being:

$$\min(obj_M(\tilde{\mu})) = obj_M(\tilde{\mu})|_{\tilde{\mu}=Y_M} = 1 + \log(\tilde{\sigma}) \tag{16}$$

Next, we examine the situation where the model predicts the minimum value $Y_m = \min\{Y_1, Y_2, \dots, Y_n\}$. In this case, Y_m follows a minimum distribution, whose probability density function is (Cai & Hames, 2010):

$$f(Y_m) = \frac{1}{\tilde{\sigma}} \exp\left(\frac{Y_m - \tilde{\mu}}{\tilde{\sigma}} - \exp\left(\frac{Y_m - \tilde{\mu}}{\tilde{\sigma}}\right)\right) \tag{17}$$

where $\tilde{\mu}$ and $\tilde{\sigma}$ are its position and scale parameter respectively. When making predictions for the extreme value Y_m , the optimization objective is:

$$\begin{aligned}
& \underset{\theta}{\operatorname{argmin}} -\log (P(Y_m|\tilde{\mu}, \tilde{\sigma})) \\
&= \underset{\theta}{\operatorname{argmin}} -\frac{Y_m - \tilde{\mu}}{\tilde{\sigma}} + \exp\left(\frac{Y_m - \tilde{\mu}}{\tilde{\sigma}}\right) + \log(\tilde{\sigma}) \\
& \text{where } \tilde{\mu} \equiv \min\{F_{\theta}(X_1), F_{\theta}(X_2), \dots, F_{\theta}(X_n)\}
\end{aligned} \tag{18}$$

Denote the optimization objective as $obj_m(\cdot)$

$$obj_m(\tilde{\mu}) = -\frac{Y_m - \tilde{\mu}}{\tilde{\sigma}} + \exp\left(\frac{Y_m - \tilde{\mu}}{\tilde{\sigma}}\right) + \log(\tilde{\sigma}) \tag{19}$$

Similar to the analysis process of $obj_M(\cdot)$, we can prove that $obj_m(\cdot)$ first decreases and then increases. The minimum value of $obj_m(\cdot)$ is:

$$\min(obj_m(\tilde{\mu})) = obj_m(\tilde{\mu})|_{\tilde{\mu}=Y_m} = 1 + \log(\tilde{\sigma}) \quad (20)$$

By visualizing the shapes of $obj_M(\cdot)$ and $obj_m(\cdot)$, we gain a clearer insight into their respective characteristics.

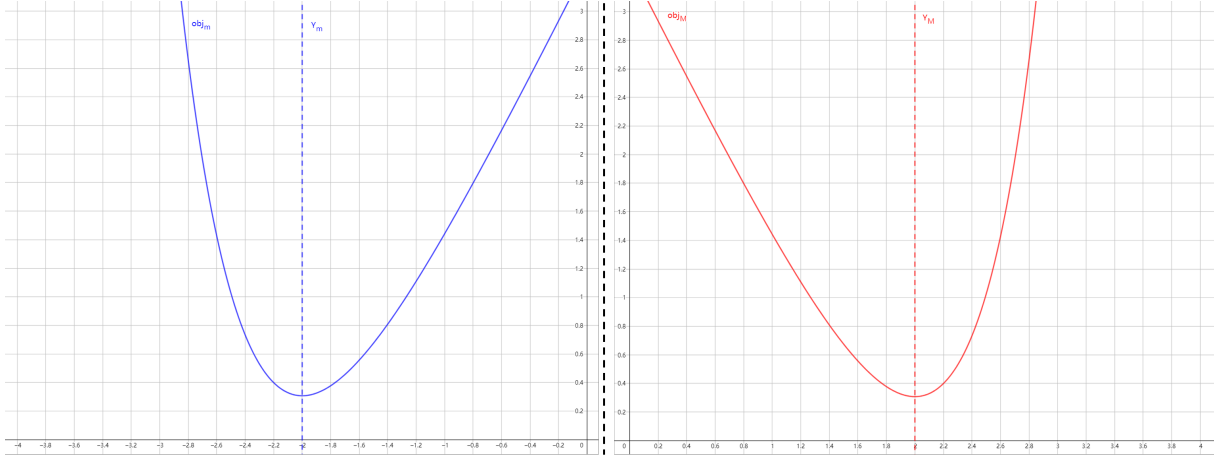


Figure 9. Visualization of Optimization Functions. The left figure is $obj_m(\cdot)$ when $Y_m = -2$ and $\sigma = 1/2$. The right figure is $obj_M(\cdot)$ when $Y_M = 2$ and $\sigma = 1/2$. The x-coordinate represents $\tilde{\mu}$ predicted by the model.

It can be seen from Figure 9 that both $obj_m(\cdot)$ and $obj_M(\cdot)$ are asymmetric.

A.2. Scaling Function

$obj_M(\cdot)$ and $obj_m(\cdot)$ can actually be regarded as loss functions that take into account the distribution characteristics of the original data (Wang et al., 2020b). Under this assumption, the area enclosed by the function and the x-coordinate axis can be regarded as the expectation of the total loss of this part of the sample (Hernández-Orallo et al., 2012).

We hope that the areas of $obj_M(\cdot)$ near Y_M are equal, thereby ensuring that the expectations of the total loss when underestimating extreme values and overestimating extreme values are equal. The same goes for $obj_m(\cdot)$. This goal is accomplished through scaling. Formally, for $obj_M(\cdot)$, it can be written:

$$\begin{aligned} \tilde{\mu}_s &= \begin{cases} \frac{\tilde{\sigma}}{s_1}(\tilde{\mu} - Y_M) + Y_M, & \tilde{\mu} \leq Y_M \\ \frac{\tilde{\sigma}}{s_2}(\tilde{\mu} - Y_M) + Y_M, & \tilde{\mu} > Y_M \end{cases} \\ \text{s.t. } \int_{\tilde{\mu}_s=Y_M-\epsilon}^{Y_M} obj_M(\tilde{\mu}_s) d\tilde{\mu}_s &= \int_{\tilde{\mu}_s=Y_M}^{Y_M+\epsilon} obj_M(\tilde{\mu}_s) d\tilde{\mu}_s \end{aligned} \quad (21)$$

To simplify the calculation, we subtract the minimum value of $obj_M(\cdot)$, which is $1 + \log(\tilde{\sigma})$, from $obj_M(\cdot)$. This adjustment ensures that the lowest value of $obj_M(\cdot)$ becomes 0, as shown in Figure 10. We can then compute the area around the lowest point by performing integration:

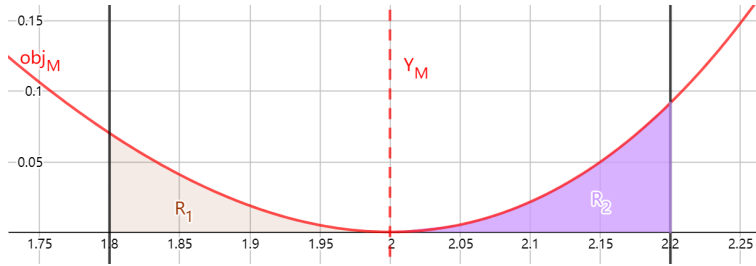


Figure 10. We hope that by scaling, the area of R_1 will be the same as R_2 .

The area integral of R_1 is as follows:

$$\begin{aligned} &\int_{\tilde{\mu}_s=Y_M-\frac{\tilde{\sigma}}{s_1}\epsilon}^{Y_M} obj_M(\tilde{\mu}_s) d\tilde{\mu}_s, \tilde{\mu}_s = \frac{\tilde{\sigma}}{s_1}(\tilde{\mu} - Y_M) + Y_M \\ &= \int_{\tilde{\mu}=Y_M-\epsilon}^{Y_M} \left(\frac{Y_M - \left(\frac{\tilde{\sigma}}{s_1}(\tilde{\mu} - Y_M) + Y_M \right)}{\tilde{\sigma}} + \exp \left(-\frac{Y_M - \left(\frac{\tilde{\sigma}}{s_1}(\tilde{\mu} - Y_M) + Y_M \right)}{\tilde{\sigma}} \right) - 1 \right) d\left(\frac{\tilde{\sigma}}{s_1}(\tilde{\mu} - Y_M) + Y_M \right) \\ &= \frac{\tilde{\sigma}}{s_1} \int_{\tilde{\mu}=Y_M-\epsilon}^{Y_M} \left(\frac{Y_M - \tilde{\mu}}{s_1} + \exp \left(-\frac{Y_M - \tilde{\mu}}{s_1} \right) - 1 \right) d\tilde{\mu} \\ &= \frac{\tilde{\sigma}}{s_1} \left(-\frac{s_1}{2} \left(\frac{Y_M - \tilde{\mu}}{s_1} \right)^2 + s_1 \cdot \exp \left(-\frac{Y_M - \tilde{\mu}}{s_1} \right) - \tilde{\mu} \right) \Big|_{Y_M-\epsilon}^{Y_M} \\ &= \tilde{\sigma} \left(\frac{\epsilon^2}{2s_1^2} - \frac{\epsilon}{s_1} - \exp \left(-\frac{\epsilon}{s_1} \right) + 1 \right) \end{aligned} \quad (22)$$

The area integral of R_2 is as follows:

$$\begin{aligned}
& \int_{\tilde{\mu}_s=Y_M}^{Y_M+\frac{\tilde{\sigma}}{s_2}\epsilon} obj_M(\tilde{\mu}_s) d\tilde{\mu}_s, \tilde{\mu}_s = \frac{\tilde{\sigma}}{s_2}(\tilde{\mu} - Y_M) + Y_M \\
&= \int_{\tilde{\mu}=Y_M}^{Y_M+\epsilon} \left(\frac{Y_M - \left(\frac{\tilde{\sigma}}{s_2}(\tilde{\mu} - Y_M) + Y_M \right)}{\tilde{\sigma}} + \exp \left(-\frac{Y_M - \left(\frac{\tilde{\sigma}}{s_2}(\tilde{\mu} - Y_M) + Y_M \right)}{\tilde{\sigma}} \right) - 1 \right) d \left(\frac{\tilde{\sigma}}{s_2}(\tilde{\mu} - Y_M) + Y_M \right) \\
&= \frac{\tilde{\sigma}}{s_2} \int_{\tilde{\mu}=Y_M}^{Y_M+\epsilon} \left(\frac{Y_M - \tilde{\mu}}{s_2} + \exp \left(-\frac{Y_M - \tilde{\mu}}{s_2} \right) - 1 \right) d\tilde{\mu} \\
&= \frac{\tilde{\sigma}}{s_2} \left(-\frac{s_2}{2} \left(\frac{Y_M - \tilde{\mu}}{s_2} \right)^2 + s_2 \cdot \exp \left(-\frac{Y_M - \tilde{\mu}}{s_2} \right) - \tilde{\mu} \right) \Big|_{Y_M}^{Y_M+\epsilon} \\
&= \tilde{\sigma} \left(-\frac{\epsilon^2}{2s_2^2} - \frac{\epsilon}{s_2} + \exp \left(\frac{\epsilon}{s_2} \right) - 1 \right)
\end{aligned} \tag{23}$$

In order to achieve equality between the areas of R_1 and R_2 , we obtain the following equation:

$$\begin{aligned}
& \tilde{\sigma} \left(\frac{\epsilon^2}{2s_1^2} - \frac{\epsilon}{s_1} - \exp \left(-\frac{\epsilon}{s_1} \right) + 1 \right) = \tilde{\sigma} \left(-\frac{\epsilon^2}{2s_2^2} - \frac{\epsilon}{s_2} + \exp \left(\frac{\epsilon}{s_2} \right) - 1 \right) \\
& \frac{\epsilon^2}{2s_1^2} + \frac{\epsilon^2}{2s_2^2} - \frac{\epsilon}{s_1} + \frac{\epsilon}{s_2} - \exp \left(-\frac{\epsilon}{s_1} \right) - \exp \left(\frac{\epsilon}{s_2} \right) + 2 = 0
\end{aligned} \tag{24}$$

The parameter ϵ is associated with the prediction accuracy. The higher the prediction accuracy is, the smaller the error is. The closer the predicted $\tilde{\mu}$ will be to the real target Y_M , the smaller the area we need to consider, that is, the smaller ϵ will be. On the contrary, when the prediction accuracy is very low, the $\tilde{\mu}$ predicted by the model is relatively far away from Y_M , so the ϵ we need to consider must be appropriately increased.

In the actual training, we select $\epsilon = 0.1\tilde{\sigma}$ as our choice, because of the observation that the relative error of the model's predictions for extreme values is often below 10% (Bellprat & Doblas-Reyes, 2016) (Fang et al., 2021). Therefore it is sufficient to consider an error margin of 10%. On the other hand, if the error range considered is too small, the scaling effect will not be obvious. When we set $\epsilon = 0.1\tilde{\sigma}$, the solution to Equation (24) remains non-unique. Since our primary interest lies in the relative relationship between s_1 and s_2 , it is reasonable to fix one of them first. We fix s_2 to $\tilde{\sigma}$, and calculate that $s_1 = 0.9\tilde{\sigma}$ approximately.

Thus we can obtain the specific form of the scaling function, depicted below::

$$\tilde{\mu}_s = \begin{cases} \frac{10}{9}(\tilde{\mu} - Y_M) + Y_M, & \tilde{\mu} \leq Y_M \\ \tilde{\mu}, & \tilde{\mu} > Y_M \end{cases} \tag{25}$$

Subtract Y_M from both sides to get:

$$\begin{aligned}
\tilde{\mu}_s - Y_M &= \begin{cases} \frac{10}{9}(\tilde{\mu} - Y_M), & \tilde{\mu} \leq Y_M \\ \tilde{\mu} - Y_M, & \tilde{\mu} > Y_M \end{cases} \\
(\tilde{\mu}_s - Y_M)^2 &= \begin{cases} \frac{100}{81}(\tilde{\mu} - Y_M)^2, & \tilde{\mu} \leq Y_M \\ (\tilde{\mu} - Y_M)^2, & \tilde{\mu} > Y_M \end{cases}
\end{aligned} \tag{26}$$

Similarly, for the prediction of minimum values Y_m , we can also apply a similar scaling function:

$$(\tilde{\mu}_s - Y_m)^2 = \begin{cases} \frac{100}{81}(\tilde{\mu} - Y_m)^2, & \tilde{\mu} \geq Y_m \\ (\tilde{\mu} - Y_m)^2, & \tilde{\mu} < Y_m \end{cases} \tag{27}$$

Finally, merge the two scaling functions into $S(\hat{Y}, Y)$:

$$S(\hat{Y}, Y) = \begin{cases} \frac{100}{81}, & (\hat{Y} \geq Y \text{ and } Y < Y_{10th}) \text{ or } (\hat{Y} \leq Y \text{ and } Y > Y_{90th}) \\ 1, & \text{else} \end{cases} \quad (28)$$

where \hat{Y} is the prediction and Y is the target. Y_{10th} and Y_{90th} correspond to the 10th and 90th percentiles in the sample, respectively, and they can serve as thresholds for extreme values (such as extremely low or high temperatures). The expression $(\hat{Y} \geq Y \text{ and } Y < Y_{10th}) \text{ or } (\hat{Y} \leq Y \text{ and } Y > Y_{90th})$ refers to the situation where the true value meets the threshold of extreme values, but the model gives an underestimated prediction. By applying the scaling function $S(\cdot)$ to the loss function, we obtain Exloss. It is noticeable that the model increases the loss when underestimating extremes, thereby imposing a higher penalty.

$$\text{Exloss}(\hat{Y}, Y) = \|S(\hat{Y}, Y) \odot (\hat{Y} - Y)\|^2 \quad (29)$$

A.3. ExEnsemble

The python code of ExEnsemble (pytorch implementation) is implemented as follows:

```

def SortIndex(input):
    """
    Get the sorting ranking corresponding to each element in tensor.
    Args:
        input (torch.Tensor): The input tensor.
    Returns:
        torch.Tensor: Tensor of the same size as input. The ranking of each element in the
                      tensor, from smallest to largest.
    Example:
        input=torch.tensor([1.2, 1.5, 0.8, 0.9])
        return torch.tensor([2, 3, 0, 1])
    """
    sorted_indices = torch.argsort(input, dim=-1)
    ranks = torch.argsort(sorted_indices, dim=-1)
    return ranks

```



```

def ExEnsemble(pred, ensembles_nums=50, ensembles_scale=0.1):
    """
    Apply ExEnsemble to the predictions.
    Args:
        pred (torch.Tensor): Tensor of size [B, C, H, W]. The input predictions.
        ensembles_nums (int): Number of ensembles (default: 50).
        ensembles_scale (float or torch.Tensor): Scaling factor for ensembles. It can be a
                                                real number or a tensor of size [B,
                                                C, H, W] (default: 0.1).
    Returns:
        torch.Tensor: Tensor of size [B, C, H, W]. The ensemble boosted predictions.
    """
    B, C, H, W = pred.shape

    scale = ensembles_scale * torch.ones_like(pred) # [B, C, H, W]

    # Get index
    idx = SortIndex(pred.flatten(2,3)) # [B, C, H*W]

    # Sample
    pred = pred.unsqueeze(2) # [B, C, 1, H, W]
    scale = scale.unsqueeze(2) # [B, C, 1, H, W]
    disturbance = torch.randn(B, C, ensembles_nums, H, W, device=pred.device) * scale
    ens = pred + disturbance # [B, C, ensembles_nums, H, W]

    # Sort ensembles
    sorted_ens, _ = torch.sort(ens.flatten(2,4)) # [B, C, ensembles_nums*H*W]
    sorted_ens = sorted_ens.reshape(B, C, H*W, ensembles_nums) # [B, C, H*W,
                                                               ensembles_nums]

    # Partition and median
    k = int(0.5 * ensembles_nums) # ensembles_nums / 2
    sorted_ens_mid, _ = torch.kthvalue(sorted_ens, k, -1) # [B, C, H*W]

    # Restore by index
    ens_from_idx = torch.gather(sorted_ens_mid, dim=-1, index=idx) # [B, C, H*W]
    out = ens_from_idx.reshape(B, C, H, W) # [B, C, H, W]

    return out

```

A.4. Training Details

Our model is trained for 2 weeks using 32 A100 GPUs, and the batch size is 32. The number of learnable parameters of M_d are 570M, the learning rate of stage 1 is 2.5e-4, and the learning rate of stage 2 is 5e-6. The number of learnable parameters of M_g are 140M, and the learning rate is 5e-4.

As mentioned in Section 3.2, we will use Exloss in Stage 2 and Stage 3 of model training.

In Stage 2, the model will perform multi-step autoregressive fineutne on M_d through the replay buffer (Chen et al., 2023a). We employ Exloss as the loss function in this stage to help the model achieve accurate multi-step predictions for extreme weather events.

In Stage 3, We freeze the parameters of M_d and train the diffusion model M_g to generate the land-surface variables (u10, v10, t2m) with more details. In order to further improve the expression of diffusion for extreme values, we apply Exloss in diffusion to directly optimize extreme values and avoid losing details as prediction time increases.

$$Loss(\hat{\varepsilon}, \varepsilon) = \|\hat{\varepsilon} - \varepsilon\|^2 + Exloss(\hat{\varepsilon}, \varepsilon) \quad (30)$$

where $\hat{\varepsilon}$ and ε represent the predicted Gaussian noise (Yang et al., 2023) and the actual added noise in diffusion.

Finally, concatenate the not-land-surface variables (msl, z, q, u, v, t) of M_d 's output with the land-surface variables of M_g 's output to obtain more detailed forecasts.

A.5. Module Processing Visualization

As described in Section 3.2, our model comprises two trainable modules, namely the deterministic model (denoted as M_d) and the probabilistic generation model (denoted as M_g), along with the training-free ExEnsemble module. The outputs of these modules are denoted as P_d , P_g , and P_e respectively. By visualizing the difference between P_g and P_d , we can observe the impact of the diffusion model, while visualizing the difference between P_e and P_g allows us to examine the effect of the ExEnsemble module.

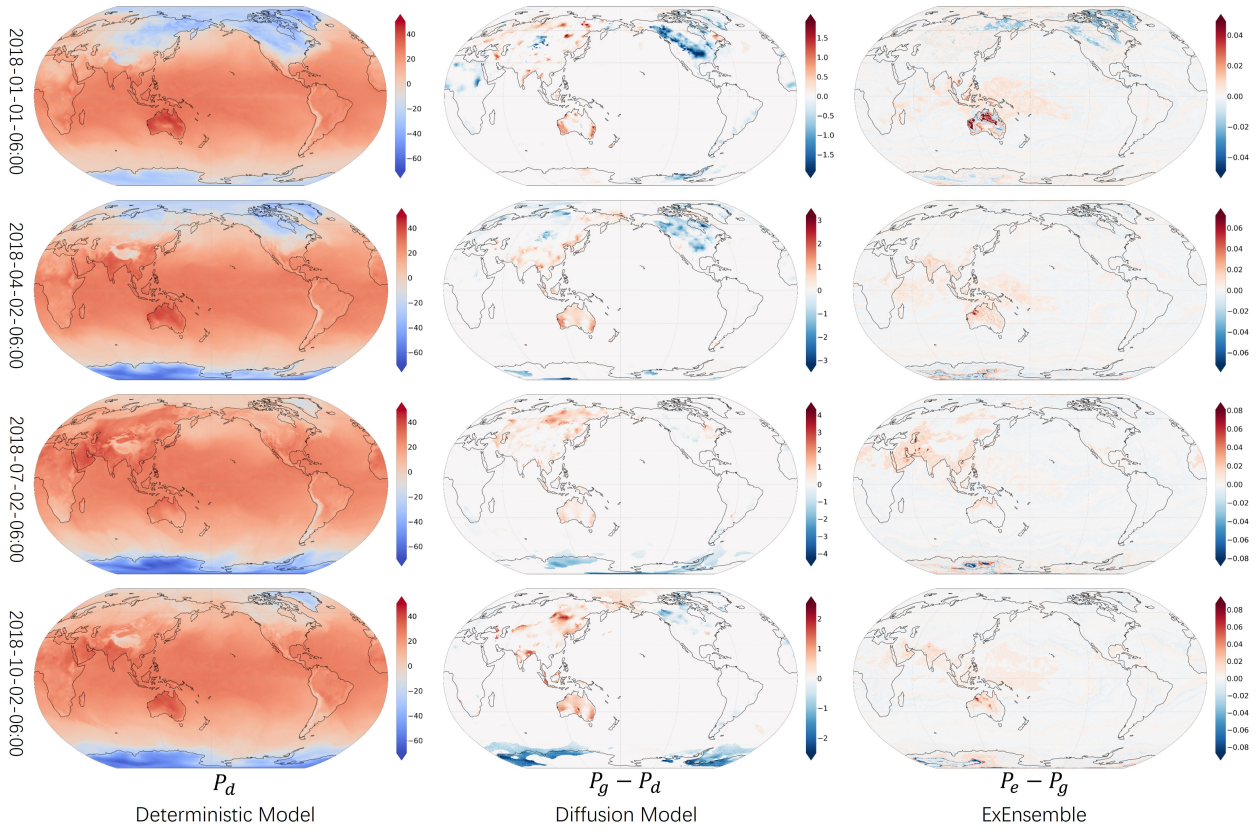


Figure 11. Processing of Different Modules of t2m.

Two key observations can be derived from Figure 11. Firstly, both the diffusion and ExEnsemble modules exert similar influences on the final output. This indicates that our distinct modules show consistency and do not adversely affect one another. Secondly, both the diffusion and ExEnsemble modules result in increased temperatures in mid-latitudes and decreased temperatures in high-latitudes (Richard et al., 2013) (Francis & Vavrus, 2012). Collectively, this contributes to a certain level of extreme weather events at the global scale.

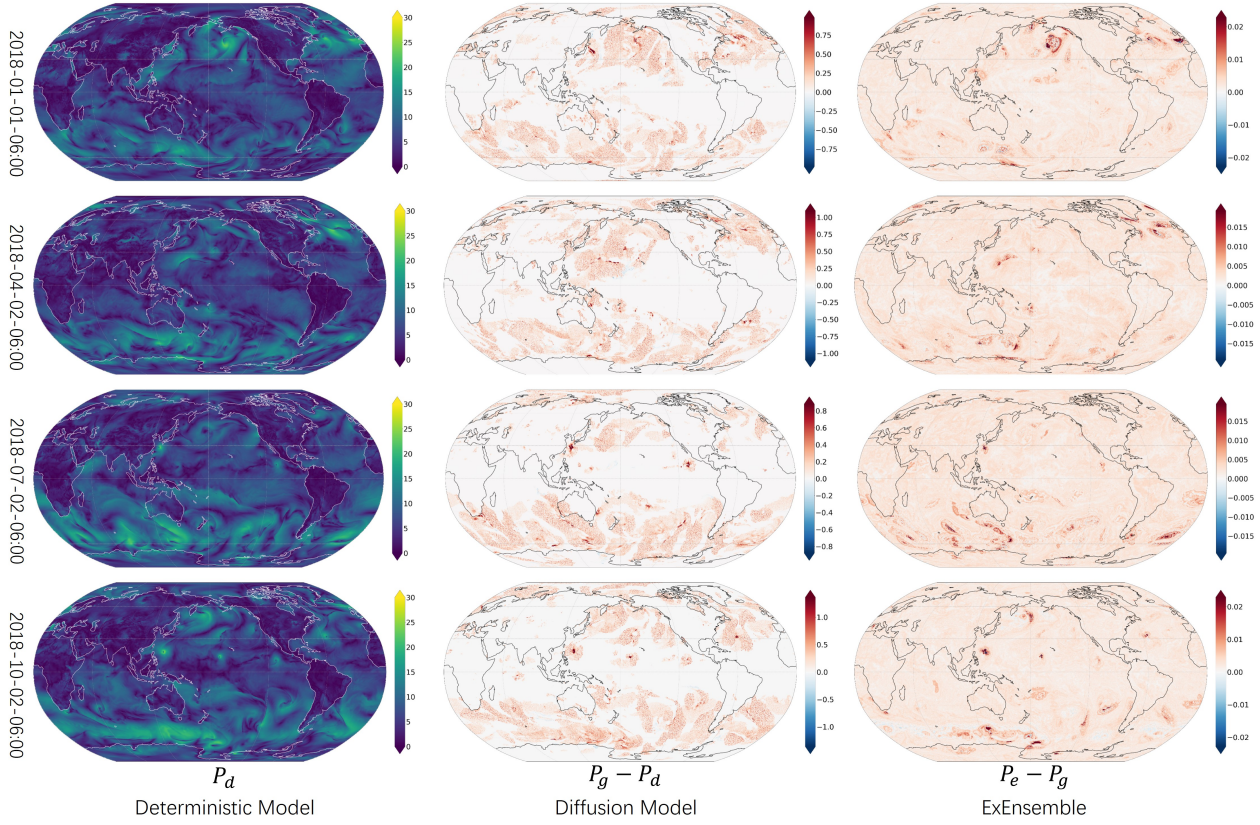


Figure 12. Processing of Different Modules of ws10.

As depicted in Figure 12, both the diffusion and ExEnsemble modules exhibit an amplifying effect on wind speed, consequently leading to an increase in extreme wind speed. Furthermore, in the vicinity of cyclones (Gray, 1977) exhibiting higher wind speeds, we observe a pronounced intensification of the enhancement effect facilitated by the diffusion and ExEnsemble modules. This notable enhancement is particularly advantageous in the accurate prediction of typhoons and their associated wind speeds (Wei et al., 2018) (Yang & Tsai, 2019).